J Seismol (2025) 29:661–676
https://doi.org/10.1007/s10950-025-10298-9

RESEARCH

Multiscale regionalised Rayleigh-wave group and phase velocity maps for East Asia

Mei Feng · **Meijian An** · **Hesheng Hou** ·
Rongtao Zhao

Received: 5 February 2025 / Accepted: 14 May 2025 / Published online: 6 June 2025

Abstract East Asia comprises multiple tectonic domains and has been the subject of many regional and local broadband seismic investigations in recent years, especially the ChinArray experiments. These studies have improved the overall seismic data coverage for East Asia, although the distribution of data is extremely uneven. While regionalised group or phase velocity dispersion curves from surface-wave tomography are particularly important for deriving deep shear-wave velocities, calibrating phase velocity measurements and joint analyses with other geophysical data, they are normally derived using quadrilateral cells with a fixed latitude and longitude spacing, such that the cell spacing varies with latitude but not with data coverage. For a region with extremely uneven data coverage, closely spaced cells will worsen the ill-posedness of tomographic problems, whereas widely spaced cells will lower the lateral resolution capability of regions with dense data. Here we propose a new model discretisation approach for two-dimensional surface-wave tomography that divides the study area into triangular cells with variable sizes based on data coverage and apply it to East Asia, where seismic observations are numerous but unevenly distributed. The updated regionalised Rayleigh-wave group and phase velocity maps detect small sedimentary basins with low velocities and large cratons with high velocities, implying that our approach can simultaneously image local-, regional- and large-scale structures in one tomographic system. The regionalised dispersion curves can be used to invert for deep structure directly or jointly with other geophysical observations across East Asia.

Highlights

- The Rayleigh-wave velocities of earthquake and noise data recorded by 2917 new stations in East Asia are processed.
- Two-dimensional surface-wave tomography using a variable cell size based on data coverage enables the imaging of multiscale structures.
- The updated multiscale regionalised dispersion curves are indispensable for future and/or joint studies in East Asia.

Keywords Rayleigh-wave tomography · Regionalised group and phase velocity · Triangular cell · Variable-size cells · East Asia

---

Supplementary Information The online version contains supplementary material available at https://doi.org/10.1007/s10950-025-10298-9.

M. Feng (✉) · M. An · H. Hou · R. Zhao
Chinese Academy of Geological Sciences, No. 26
Baiwanzhuang Street, Beijing 100037, China
e-mail: mei_feng_cn@163.com

1 Introduction

East Asia comprises a variety of tectonic domains (Fig. 1a), including the world's highest plateau (Qinghai–Tibetan Plateau), deepest trench (Mariana Trench), largest accretionary orogenic belt (Central Asian Orogenic Belt), most complex multi-directional subduction belt (Philippine Subduction Belt) and most intensively deformed Archean craton (North China Craton) (Yin 2010; Ren et al. 2013). Consequently, many broadband seismic studies have sought to characterise the deep Earth structure of East Asia, including phases I–IV of INDEPTH (Kind et al. 2002; Tilmann et al. 2003; Zhao et al. 2011), Hi-CLIMB (Wittlinger et al. 2009), HIMNT (De La Torre et al. 2007), ASCENT (Yue et al. 2012) and LMSF (Qian et al. 2018, 2022), all of which were deployed in and around the Qinghai–Tibetan Plateau; NECESSArray (Tao et al. 2014) and NECsaids (Wang et al. 2016; Zhang et al. 2020) deployed in and around Northeast China; QinSeisArray deployed in the Qinling Orogenic Belt and Ordos Basin in central-north China (Feng et al. 2017); several phases of NCISP deployed in and around the North China Craton (Wei et al. 2011; Chen et al. 2014); and the two phases of ChinArray (Chang et al. 2017; Zhang et al. 2018), which were focussed on the North–South Seismic Belt of Central China. Whilst these seismic observations have improved the coverage of seismic data in East Asia, the data coverage is extremely uneven.

Two-dimensional surface-wave tomography provides regionalised surface-wave velocities at given discrete cells along the source-to-station or station-to-station paths. The regionalised velocities are particularly important in deriving deep shear-wave velocities, calibrating phase velocity measurements and subsequent joint analyses with receiver functions (Julià et al. 2000; Lloyd et al. 2010; Sun et al. 2014; Rodríguez Kacevas et al. 2024), body-wave travel times (Chang et al. 2010; Han et al. 2022), gravity data (Maceira and Ammon 2009; Syracuse et al. 2017; Carrillo et al. 2024) and magnetotelluric data (Moorkamp et al. 2010; Roux et al. 2011; Wu et al. 2020). Surface-wave tomography has therefore

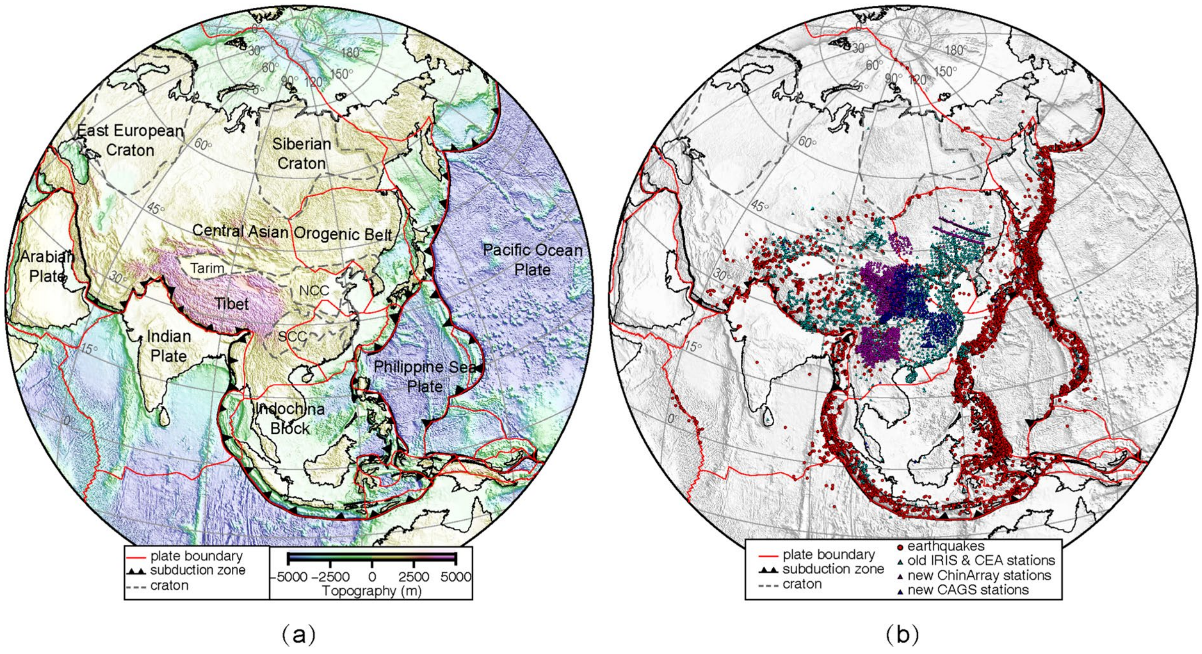

Fig. 1 (**a**) Simplified geotectonic map of East Asia and (**b**) map showing the locations of seismic stations (triangles) and earthquakes (red circles) used in this study. The tectonic plate boundaries are from Bird (2003). The cyan triangles in (b) denote stations with open-access data from IRIS and CEA that have been processed by the present authors in previous studies (An et al. 2009; Feng and An 2010; Feng et al. 2011, 2020, 2023a, 2023b); magenta and blue triangles denote stations with non-open-access data from ChinArray and from CAGS that have been processed in the current study

been widely applied to explore the Earth's structure at various scales, including global (Trampert and Woodhouse 1995, 2001; Nishida et al. 2009; Ma et al. 2014), regional (Ritzwoller and Levshin 1998; Vdovin et al. 1999; Moschetti et al. 2007; Boué et al. 2014; Li and Fu 2020; Fan et al. 2023) and local scales (Cho et al. 2007; Ramos et al. 2016; Feng et al. 2021). Most tomographic methods employ quadrilateral cells with equal latitude and longitude spacings. This type of model discretisation simplifies conventional tomographic processing, including travel-time calculations, regularisations and checkerboard resolution tests. However, since the uneven distribution of data coverage cannot be considered, the model discretisation often matches the average resolvable level of data coverage (e.g., Fishwick 2010; Isse et al. 2019) and does not reflect the true lateral resolution in areas with good data coverage. Therefore, using cells of variable size based on the data coverage can optimise the lateral resolution of the tomographic results, especially for regions such as East Asia where the data coverage is extremely uneven.

Model discretisation with cells of variable size has previously been investigated, including in body-wave tomography (Abers and Roecker 1991; Thurber and Eberhart-Phillips 1999; Hansen et al. 2012, 2014). Variable-size cells in body-wave tomography can be achieved by merging one or more basic-sized quadrilateral cells based on data coverage (Hansen et al. 2012). Variable-size cells have also been applied in surface-wave tomography (Sambridge et al. 1995; Wang and Dahlen 1995; Wang et al. 1998; Schaefer et al. 2011; Li and Lin 2014; Lu et al. 2018; Magrini et al. 2022), with Sambridge et al. (1995) and Li and Lin (2014) employing Delaunay triangulation. However, the discretisation of Delaunay triangulation makes it difficult to evaluate the resolution via a checkerboard test, which is a common way to assess model resolvability. Other studies have attempted to split basic quadrilateral cells one or more times according to data coverage to achieve variable-size cells in surface-wave tomography (Schaefer et al. 2011; Lu et al. 2018; Magrini et al. 2022). However, a basic quadrilateral cell with equal latitude and longitude spacings is not equidistant across different latitudes, with this disparity becoming greater in high-latitude regions. Therefore, quadrilateral cells with either fixed or variable sizes have poor applicability in high-latitude regions, such as polar or global areas. For example, Zhou et al. (2022) and An et al. (2015) resorted to using coordinate transformation and equal-area hexagonal cells in their respective surface wave tomographic studies of Antarctica.

To resolve these problems, we propose an improved tomographic approach that uses variable-size triangles, adds non-uniform regularisations, and conducts quantitative resolution evaluations to simultaneously achieve global-, regional- and local-scale regionalised surface-wave dispersions in a single tomographic inversion system. The approach is applied to East Asia, where surface-wave data coverage is extremely uneven, to validate the effectiveness of this approach and update regionalised surface-wave dispersions for the region.

2 Methodology

2.1 Surface-wave tomography

Based on a series of theoretical tests, Sieminski et al. (2004) validated the feasibility of conducting surface-wave tomography based on ray theory in areas with dense data coverage as the disadvantage of considering finite frequency effects in ray theory can be balanced by proper regularisation. Surface-wave tomography based on ray theory can even detect lateral non-uniform structures at sub-wavelength scales. In practical applications, diffraction tomography based on finite frequency theory and travel time tomography based on ray theory reveal similar structures in regions with dense coverage (Ritzwoller et al. 2002). We therefore adopted the two-dimensional surface-wave tomography method based on ray theory that was proposed by Feng et al. (2004). However, it is worth noting that ray-based tomography for short periods is normally more reliable than for long periods due to the degradation of data coverage at longer periods. According to ray theory, if the study area is divided into many small cells and the wave velocity is assumed to be uniform in each cell, then the total travel time t_{obs} of any observed surface wave at a certain period can be approximated as the sum of the travel times in each cell. The slowness (reciprocal of velocity) of each cell can be obtained by minimising the weighted sum of the travel time residuals and regularisations (e.g., damping, flatness or smoothness constraints), as follows:

$$F(s) = min\left(\|G \bullet s - t_{obs}\|^2 + \lambda\|\Delta s\|^2\right) \quad (1)$$

where $\boldsymbol{G}$ contains the lengths of each ray that passes through each cell for surface waves, and is termed the sensitivity kernel matrix; $\boldsymbol{s}$ is the unknown vector containing the surface-wave slowness of each cell, which is to be determined; $\boldsymbol{t}_{\mathrm{obs}}$ is the data vector, with the total ray length divided into average wave velocities; $\boldsymbol{\Delta s}$ represents the first-order gradient of the model, also known as flatness regularisation, which mainly smooths the surface-wave slowness distribution and stabilises the inversion of large ill-posed equation systems; and λ is the regularisation factor, which can be determined by the Morozov's difference principle (Morozov 1984), whereby the best λ normally locates around the inflection point where data misfit suddenly changes with λ. Note that the larger the λ, the smoother the model (or the worse the data fit). Using the Least Squares QR method (Paige and Saunders 1982), the surface-wave slowness (or velocity) of each cell can be solved from Eq. (1).

2.2 Adaptive gridding

We use Discrete Global Grid Systems (DGGS) to divide the Earth's surface into equal-sized Delaunay triangulation cells (Sahr et al. 2003). The aperture parameter that controls the size of the triangular cell is set to 4, and the inter-cell distance is ~1.32° of great arc distance, which meets the requirement of global-scale tomography. Previous tomographic investigations would generally set the study region according to given latitude and longitude ranges, resulting in the inclusion of many cells with no data coverage. Since the DGGS method generates cells for the entire surface of the Earth, we can eliminate the cells with no data based on the actual shape of the study region.

Based on uniformly distributed triangular cells of aperture 4 (referred to as the basic cell), we performed two-dimensional ray tracing for all observations and analysed the data distribution of each cell. Specifically, we counted the measurements in each cell over the –90° to 90° azimuthal range at a given interval *dbaz*. The number of azimuthal intervals with measurements (m, $m \leq 180°/dbaz$) and the number of measurements in each azimuthal interval (n, $n > 0$) were taken as two indicators to assess the quality of data coverage of each cell. Figure 2a shows a simplified example using an azimuthal interval of 30°. The number of filled rose petals (m) corresponds to the number of azimuths with observed data, and the petal length is proportional to the data number (n) in this direction. For the example in Fig. 2a, m is 5 and the data number in the 1st (or 3rd) quadrant is larger than that in the 2nd (or 4th) quadrant. For real data, we used a finer azimuthal interval of 10°, with a maximum m of 18 (= 180°/10°).

Finally, based on the data distribution indicators (m, n) of each cell, the basic cells meeting the threshold of good data coverage (e.g., $m \geq 15$, $n \geq 1{,}000$) were partitioned into four equal-sized triangles (from one black triangle to four red triangles in Fig. 2b). Similarly, ray tracing and data distribution analysis were performed again on the partitioned cells, and the cells satisfying the threshold for good data coverage were further partitioned (from one red triangle to four blue triangles in Fig. 2b) until no cells met the threshold. We finally obtained cells composed of triangles of different sizes that were controlled by the data coverage. Note that the stricter the threshold, the fewer times the cell is partitioned. Greater partitioning means more unknown numbers to be determined, resulting in an exponential increase in the computational cost. The inter-cell distance of the basic cells is ~1.32°. This decreases to ~0.66° and ~0.33° after one and two partitions, respectively (red and blued triangles, respectively, in Fig. 2b), which can meet the requirements of regional- and local-scale surface-wave tomography. Therefore, two partitions are generally adequate in practical applications to simultaneously achieve global-, regional- and local-scale structures in a single tomographic model.

2.3 Spatially variable flatness regularisation

The use of adaptive cells can yield a cell size that provides a better match to the data distribution, although it is still impossible to ensure equal data coverage for all cells. Regularisation is therefore necessary to stabilise the ill-posed tomographic inversion. Considering the similarity of the Earth's structure beneath adjacent cells, flatness regularisation (i.e., minimising the first-order gradient of the model) is a good choice for tomographic imaging. Two triangular cells in Fig. 2d are adjacent when the two cells have at least one edge that completely or partially overlaps: two

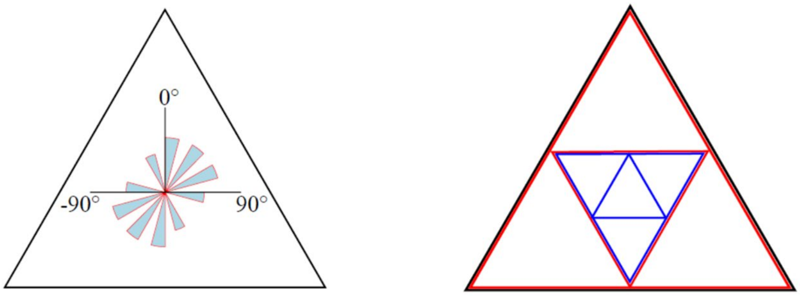

(a) Data coverage (b) Adaptive gridding

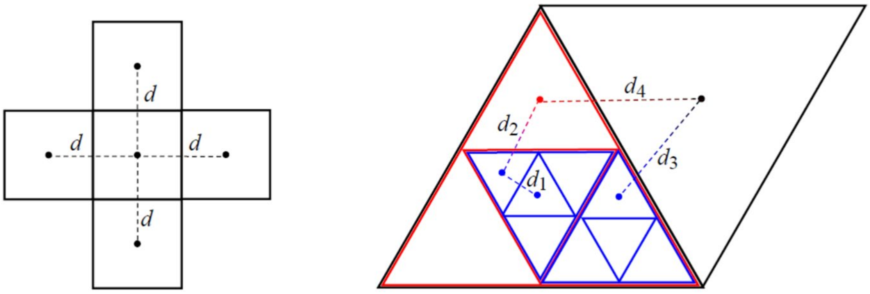

(c) Flatness for fixed-size cells (d) Flatness for adaptive cells

Fig. 2 Schematic diagram showing the definition of adaptive cells. (**a**) Indicator of data coverage; (**b**) adaptive gridding; (**c**) flatness regularisation for fixed-size cells; and (**d**) flatness regularisation for adaptive cells. The black, red and blue triangles in (b,d) are cells of different sizes. The dashes and letters (*d* or d_i) in (c,d) denote the distances between two neighbouring cell centres

cells sharing vertices but not sides are not considered adjacent.

The matrix Δs of the first-order gradient of the model in Eq. (1) is given by

$$\Delta s = \begin{pmatrix} 1 & -1 & 0 \dots & 0 \\ 0 & 1 & -1 \dots & 0 \\ 0 & 0 & 1 \dots & 0 \\ \vdots & \ddots & \ddots \ \ddots & \vdots \end{pmatrix} \tag{2}$$

where the unit coefficients 1 and –1 represent the difference between two adjacent cell parameters. The rows of the matrix correspond to each adjacent cell pair. The non-zero coefficients of different rows in Δs are all 1 or –1, which means that a uniform regularisation has been applied to all adjacent cell pairs. When using quadrilateral cells with fixed intervals, the inter-cell distance is the same throughout the entire study area (*d* in Fig. 2c) if the cell size difference caused by different latitudes is ignored, such that it is reasonable to directly employ the first-order gradient in Eq. (2) as the flatness regularisation. However, when using cells with a variable size, the inter-cell distance may be variable (d_i in Fig. 2d). Uniform regularisation will therefore force neighbouring cells with different inter-station distances to have similar velocities, which will weaken the advantage of variable-size cells in resolving structures at different scales. Since physical properties generally possess a spatial continuity, the similarity between neighbouring parameters should be related to their inter-cell distance: the smaller the inter-cell distance, the more similar they are. Introducing the reciprocal of the inter-cell distance as a weight in Eq. (2) can generate a more realistic non-uniform regularisation matrix:

$$\Delta s = \begin{pmatrix} 1/d_1 & -1/d_1 & 0 & \cdots & 0 \\ 0 & 1/d_2 & -1/d_2 & \cdots & 0 \\ 0 & 0 & 1/d_3 & \cdots & 0 \\ \vdots & \ddots & \ddots & \ddots & \vdots \end{pmatrix} \tag{3}$$

From Eq. (3), when the inter-cell distance d_i decreases, the parameters of adjacent cells will be more similar. When all d_i are equal, $1/d_i$ can be isolated as a constant coefficient of the matrix, and the regularisation matrix becomes similar to Eq. (2). The proposed definition of flatness regularisation here is more general, with flatness regularisation for fixed-size cells being a special case.

2.4 Statistical evaluation of resolution

The recovery test is a method of obtaining the resolution length by comparing the similarities or differences between the input synthetic model and output inversion solution. One of the most widely applied recovery tests in tomography is a checkerboard test (Lévěque et al. 1993), whereby the half width of the minimum recoverable checker can be taken as the resolution length (Lebedev and Nolet 2003). However, checkerboard tests are only suitable for quadrilateral cells, not triangular or hexagonal cells. To this end, An (2012) proposed a simple and universal quantitative statistical method for evaluating resolution, which was successfully applied to a tomographic study in Antarctica that used hexagonal cells. Here we give a brief introduction to the basic principles of this approach.

From a mathematical perspective, there exists the following mapping relationship between the solution vector $\underline{\boldsymbol{m}}$ of any linear problem and the real model $\boldsymbol{m}$:

$$\underline{m} = \mathfrak{R}m \tag{4}$$

where the mapping matrix $\mathfrak{R}$ is also known as the resolution matrix (Backus and Gilbert 1968, 1970). For an explicit form of Eq. (4), the mapping relation between the i-th solution $\underline{m}_i$ and the j-th real model parameter m_j can be expressed as follows:

$$\underline{m}_i = \sum_{j=1}^{k} r_{i,j} m_j \tag{5}$$

where $r_{i,j}$ is the value of the resolution matrix $\mathfrak{R}$ at the i-th row and j-th column. Equation (5) means that the i-th solution $\underline{m}_i$ is a weighted sum of the real model parameters on the j-th column, with a weighting factor $r_{i,j}$. For a tomographic problem, the real model parameters that are spatially closer to $\underline{m}_i$ have a higher weight to $\underline{m}_i$, and vice versa. The rows of $\mathfrak{R}$ can therefore be described by Gaussian functions with different widths (e.g., Nolet 2008; Fichtner and Trampert 2011; An 2012; Feng and An 2013). Half the half-height width of the Gaussian function w_i represents the width affected by the model space; i.e., the resolution length. Therefore, the problem of solving the resolution matrix $\mathfrak{R}$ is simplified to solve the width of Gaussian functions.

For any given theoretical input model $\boldsymbol{m}$, one can first obtain its corresponding solution $\underline{\boldsymbol{m}}$ via the above-described restorative experiments. Then, one can invert for the i-th row of $\mathfrak{R}$ by a Gaussian function approximation via Eq. (5). The width of the Gaussian function can be taken as the resolution length of the solution (An 2012). However, the resolution length may depend on the given input model. Therefore, the inversion of the i-th row of $\mathfrak{R}$ are done from thirty input models with random structures to meet statistical requirements (An 2012). The statistical method for evaluating the resolution using a Gaussian function approximation avoids matrix operations, simplifies calculations and avoids the influence of specific structures (e.g., checkerboard) on the resolution length. This method has been applied and validated (Feng and An 2013; Chevrot et al. 2014; Chiao et al. 2014; Ma et al. 2014, Fichtner and Leeuwen, 2015).

3 Data

To construct a more complete regionalised surface wave dispersion curve model for East Asia, we collected seismic waveforms from 8126 M> 5.0 earthquakes with average epicentral distances of ~2500–4200 km (Fig. 1b, red circles) and interstation noise data recorded by a total of 8180 seismic stations (Fig. 1b, triangles) during 1990–2024. The cyan triangles indicate 5263 old permanent and portable stations for which data are available from the IRIS Data Management Center (http://ds.iris.edu/ds/nodes/dmc/data/) and National Seismic Network Data Backup Center of the Institute of Geophysics, China Earthquake Administration (https://doi.org/10.11998/SeisDmc/SN) (Zheng et al. 2010). The magenta triangles indicate 2081 portable stations that were deployed in the North–South Seismic Belt of Central China, NE China and Mongolia by the China Earthquake Administration (CEA), with data archived in the China Earthquake Science Exploration Array Data Center (https://doi.org/10.12001/ChinArray.Data). The blue triangles represent 836 portable stations that were recently deployed in southern China, Qinling Mountains, Qilian Mountains and Longmen Mountains (Qian and Mechie 2012; Feng et al. 2017; Qu et al. 2020) by the Chinese Academy of Geological Sciences (CAGS).

The signal-to-noise ratio of Love waves is much lower than that of Rayleigh waves, and the period span is also typically shorter than that of Rayleigh waves. Therefore, we only processed the Rayleigh-wave group and phase velocities from the vertical-component seismic waves in this study. The Rayleigh-wave group velocity dispersion curves for the old permanent and portable stations (cyan triangles in Fig. 1b) are from previous studies in different regions of East Asia (An et al. 2009; Feng and An 2010; Feng et al. 2011, 2020, 2023a, 2023b). Here we measured the group velocities for the earthquake and noise data of the newly added stations (magenta and blue triangles in Fig. 1b) and phase velocities for all the stations. The group velocities of the earthquake and noise data were extracted using the multiple filtering method (Dziewonski et al. 1969), with the aid of the time–frequency analysis tool *do_mft* in the Computer Programs in Seismology package (Herrmann 2013). The phase velocities for the earthquake data were extracted using the two-station method (Ojo et al. 2018), with the aid of *sacpom96* in Computer Programs in Seismology (Herrmann 2013). The phase velocities of the inter-station noise data were extracted using a time–frequency analysis method with initial phases calibrated by given reference phase velocities (Lin et al. 2008). The reference phase velocities were estimated from a model comprising crustal structures of the CRUST1.0 model (Laske et al. 2013) and mantle structures of the IASP91 model (Kennett and Engdahl 1991).

Strict quality control was implemented to ensure the data quality of the surface-wave dispersions. Firstly, we calculated the average and standard deviation of the group or phase velocity for each period and excluded observations that exceeded twice the standard deviation. Secondly, before conducting formal tomographic imaging, an experimental inversion was conducted to eliminate data with fitting errors greater than twice the root-mean-square misfit. We finally retrieved ~ 670,100 group and ~ 369,800 phase velocity dispersion curves with a variable period spanning 10 s to 180 s. The number of observations (n) in each 10° azimuthal interval between –90° and 90° at each cell was counted. Figure 3a shows the percentage of the azimuthal distribution of the Rayleigh-wave group velocity data at the 30-s period in each basic triangular cell. The percentage is set as the number of rose petals with data coverage (m) relative to the maximum number of rose petals (= 180°/10°). The best data coverage occurs in the Tibetan Plateau

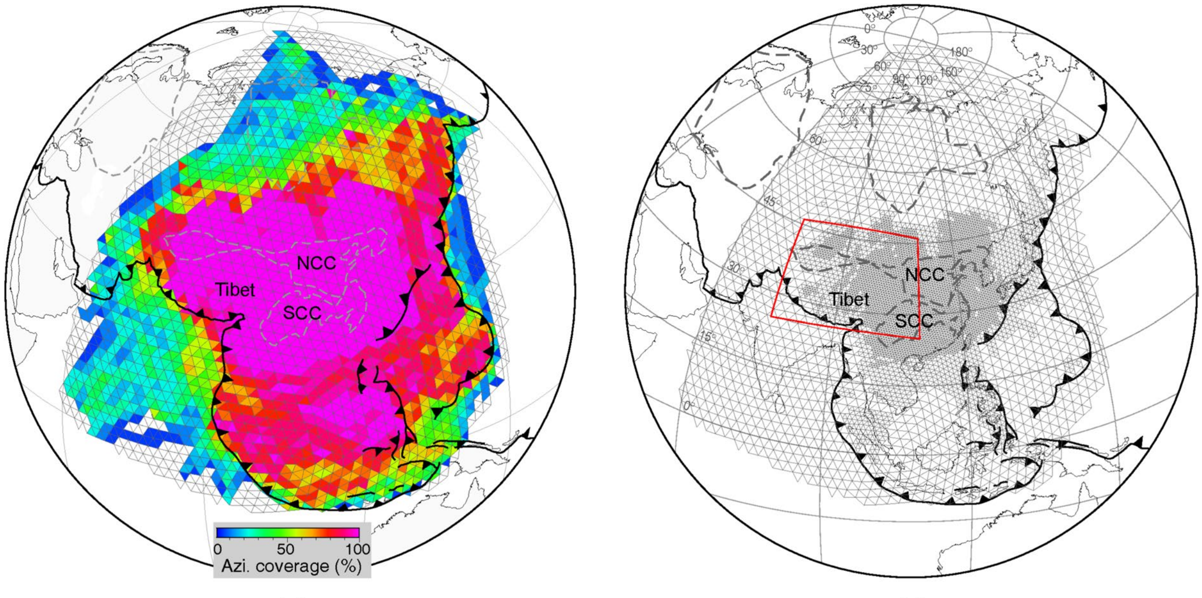

(a)

(b)

Fig. 3 (**a**) Azimuthal distributions of Rayleigh-wave group velocity observations at the 30-s period and (**b**) cells with variable sizes. The red rectangle in (b) denotes an area with three-level cells that is shown in Fig. 8

and North China Craton (NCC), and the South China Craton (SCC) (Fig. 3a). We therefore partitioned the basic triangular cells twice for those cells satisfying the ($m \geq 15$ & $n \geq 1{,}000$) and ($m = 18$ & $n \geq 1{,}000$) thresholds, and finally generated 10,430 three-level cells, as shown in Fig. 3b. Although the data distribution of the phase and group velocity varies over the analysed periods, the overall distribution is similar. To generate regionalised dispersion curves on consistent cells, both group and phase velocity tomographic inversions were performed at all periods using the same variable-size cells shown in Fig. 3b.

4 Model evaluation

A direct way to evaluate the tomographic model is to assess the degree to which the model fits the observations. Figure 4 gives four examples of the fits between the predicted and observed group and phase velocities for different regions. Both the modelled group and phase velocities fit the data well over a range of periods and ray paths (e.g., propagation through continental and oceanic tectonic environments).

The numbers of observed group and phase velocities are very large (Fig. 5a). To give a quantitative evaluation of the model, we calculated the

Fig. 4 Example data fits between observed and predicted dispersion curves. Triangles and circles represent the observed group and phase velocities, respectively, with black lines denoting predictions from two-dimensional tomographic models. The inset map shows the paths for the four sets of dispersion curves (labelled 1–4)

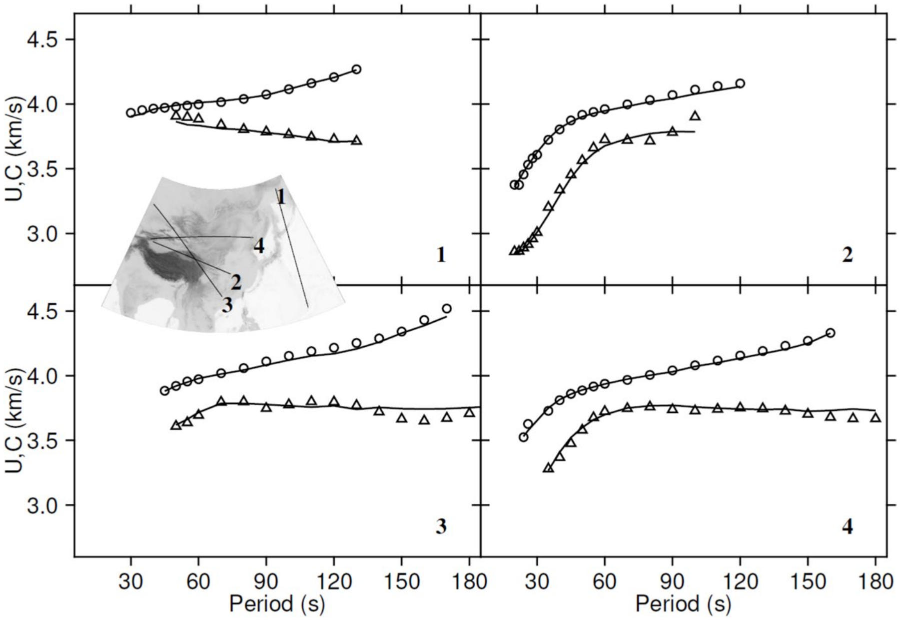

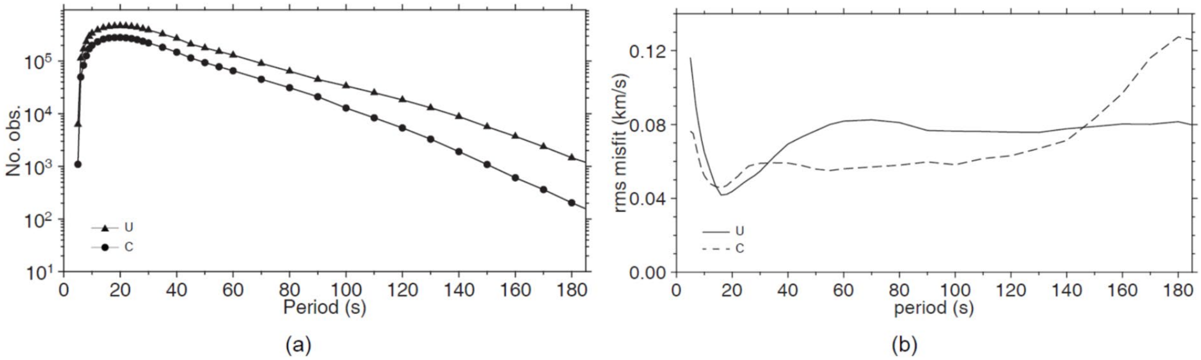

Fig. 5 (**a**) Number of observations and (**b**) root-mean-square misfit between observed and predicted data

root-mean-square misfit between all the observed and predicted data at all periods (Fig. 5b). The misfits at shorter (< 10 s) and longer (> 150 s) periods are larger than those at intermediate periods due to the limited number of observations at the former periods. The average group velocity misfit (solid line, ~0.08 km/s) is higher than the average phase velocity misfit (dashed line, ~0.05 km/s); however, both misfits are very small at all periods (< 1.4%–2.3% of the 3.5 km/s average velocity), which implies that our inverted tomographic models can fit the observations reasonably well.

Figure 6 shows the resolution lengths of the group and phase velocity tomographic models at periods of 10, 50 and 100 s. For all periods, the central region, which has better data coverage, has a better resolution (i.e., shorter length) than the surrounding region, as expected. The 50- and 100-s models have a broader range of good resolution lengths than the 10-s model because the short-period data are normally retrieved from short-path data. For the same period, the group velocity models have a broader range of good resolution lengths than the phase velocity models, as expected, since the group velocities can be measured from the stations to the teleseismic earthquakes, whereas the phase velocities can only be measured between station pairs. The consistency between the resolution and data coverage confirms the reliability of our approach to quantitatively evaluating the resolution.

A bootstrap statistical analysis was applied to estimate the uncertainties of our two-dimensional tomographic model. Thirty tomographic inversions were conducted using a random selection of 80% of the observations. The statistical standard deviation was adopted as the uncertainty of the solution. The uncertainties for the group velocity model are slightly higher than those for the phase velocity model, although most of the uncertainties are smaller than ~0.04 km/s at the 30-s period (see Figure S1 and the model file in the Supplementary Information).

5 Results and discussions

Figure 7 shows the final regionalised group and phase velocity perturbations at periods of 10, 50 and 100 s. The final tomographic model for all periods is provided in the Supplementary Information. Perturbation is measured relative to the total regional mean of each period. On the 10-s maps, which are sensitive mainly to the uppermost crustal structures, strong low velocities are observed in the major sedimentary basins or plains, including the Tarim, Ordos, Sichuan, Bohai Bay and Songliao basins, and also the back-arc basins in the West Pacific and along the Sumatra Trench, as expected.

On the 50-s maps, which are sensitive to crust–mantle transitional structures, very low velocities are found beneath the highly elevated Tibetan Plateau and Pamir Mountains, both of which possess a very thick crust. Moderately low velocities are found along the trenches where the crust may be thickened due to oceanic plate subduction. High velocities occur beneath oceanic regions, where a very thin crust is present.

On the 100-s maps, which are sensitive to mantle lithospheric structures, the cratonic regions, including the Indian Plate, Siberian Craton, Tarim Craton, Yangtze Craton and western NCC, are all characterised by high velocities, whereas the eastern margin of China and central Tibet, which have been strongly affected by the Pacific and Indian–Eurasian tectonic domains, respectively, are mainly characterised by low velocities. The phase velocity is quicker than the group velocity at the same period, and thus has a longer wavelength. This means that differences between the phase and group velocity maps at the same period inevitably exist since they are sampling structures at different depth ranges; however, the group and phase velocity maps at the same period show generally consistent structure patterns.

To show how the final regionalised dispersion curves on adaptive cells simultaneously reveal large-, intermediate- and small-scale structures, we plot the regionalised velocities in a smaller range around Tibet in Fig. 8a and along transect a–a’ in Fig. 8b–d. We also run tomographic inversions using basic cells (black triangles in Fig. 2b) and by partitioning the cells once (red triangles in Fig. 2b) for comparison. Figure 8b compares the regionalised group and phase velocities at the 50-s period along transect a–a’ for the three models using different cells. On the one hand, the regionalised velocities of the three models show generally consistent structures, confirming that the primary structural feature is not strongly affected by parameterisation. On the other hand, the velocities from the basic-cell model are strongly biased from the main feature at some neighbouring cells (black),

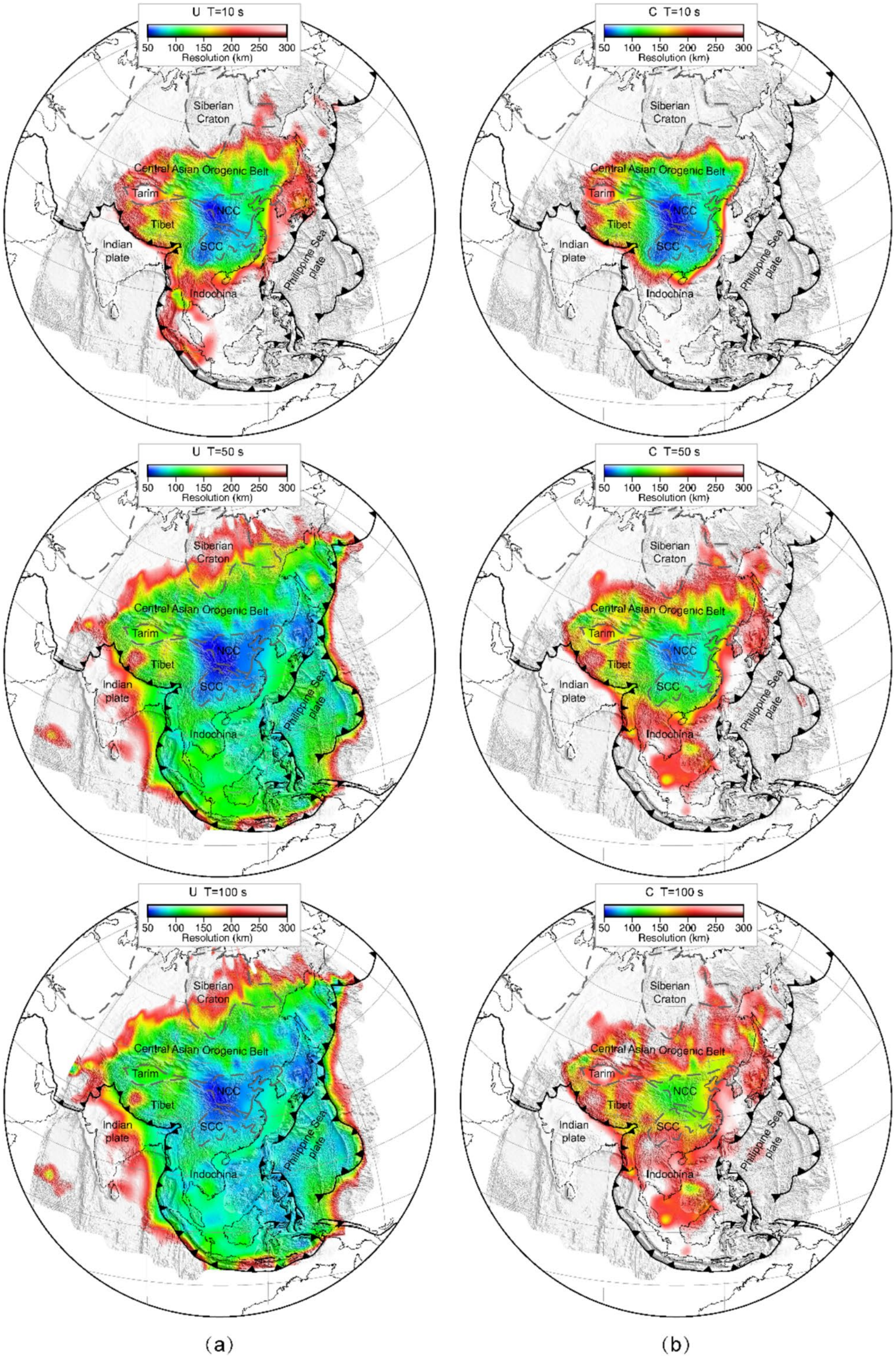

Fig. 6 Resolution length of the (**a**) group and (**b**) phase velocity tomographic models at periods of 10 s (upper), 50 s (middle) and 100 s (lower)

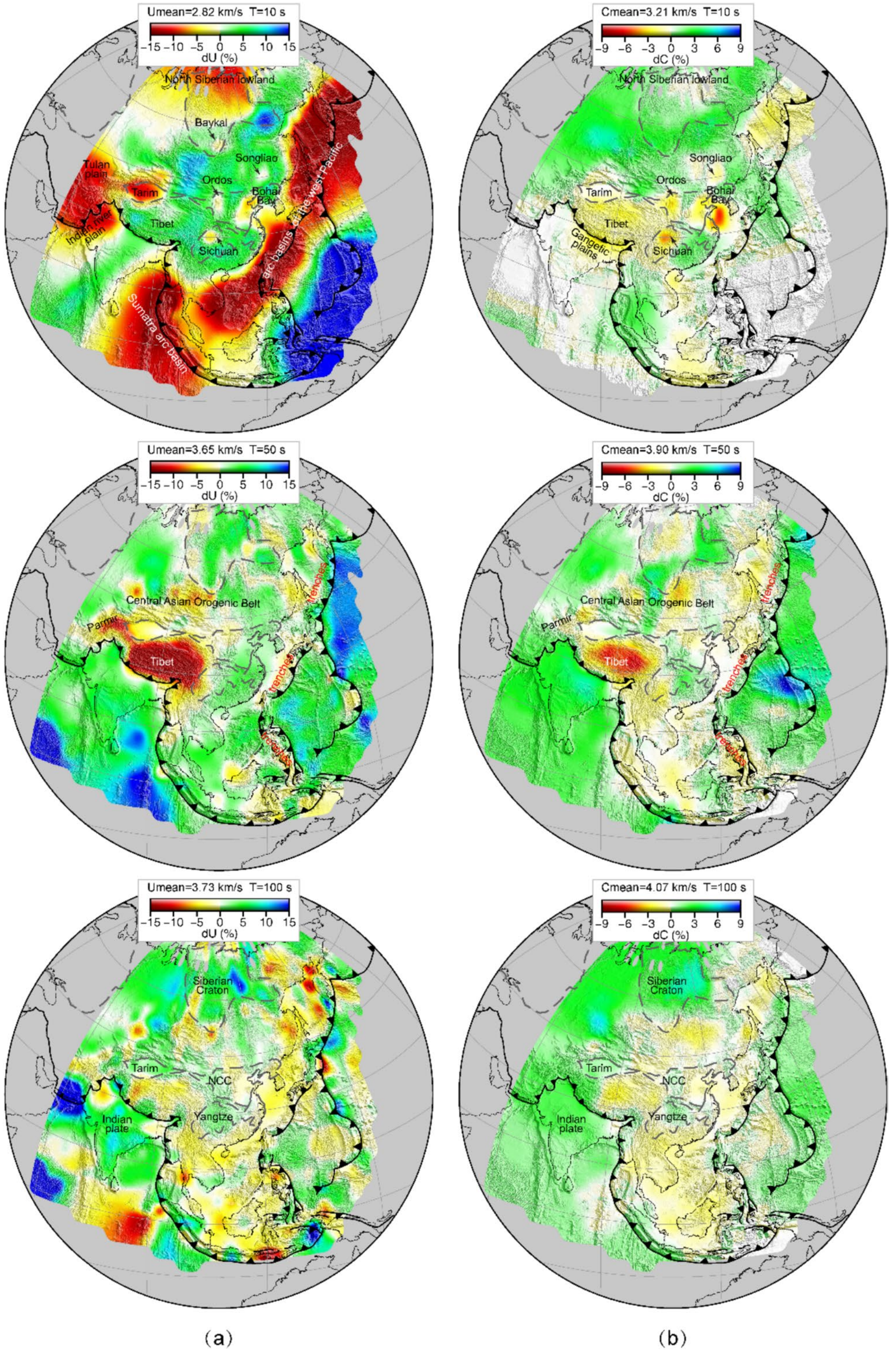

Fig. 7 Regionalised (**a**) group and (**b**) phase velocity perturbations relative to the regional mean (given above the colour bar in each subplot) at periods of 10 s (upper), 50 s (middle) and 100 s (lower)

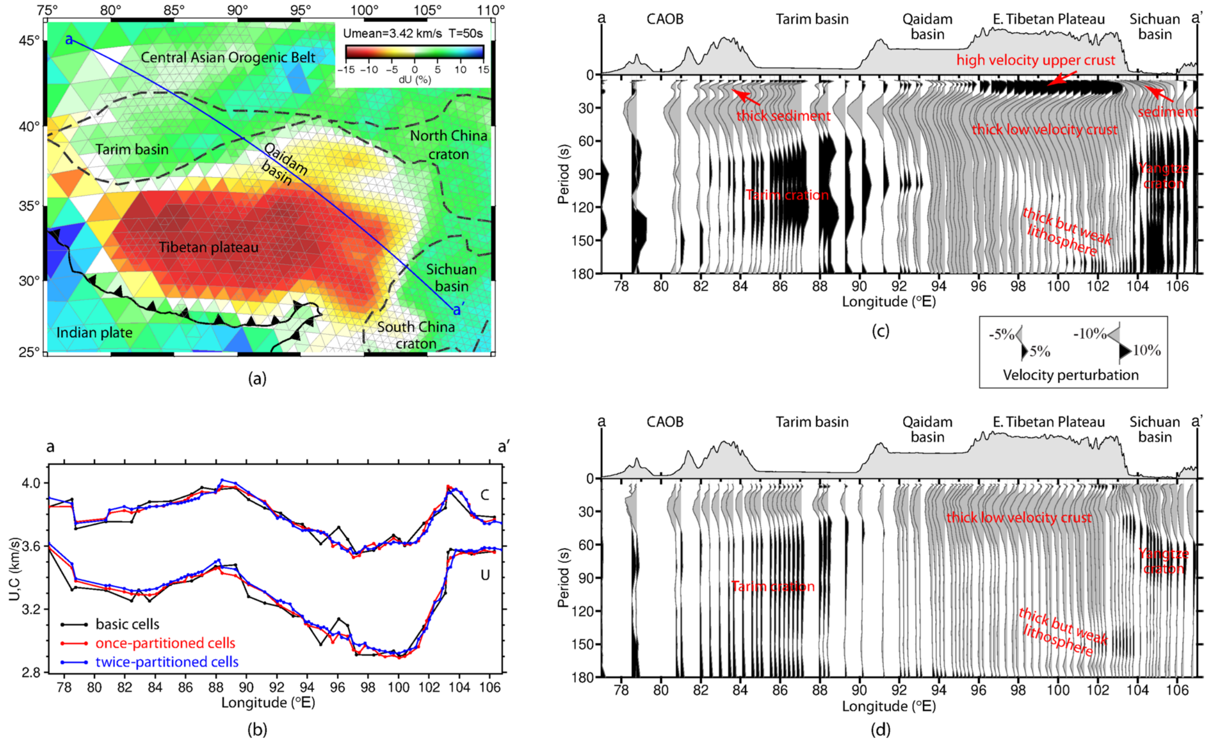

Fig. 8 Regionalised group and phase velocities along transect a–a’. (**a**) Location of transect a–a’ on the 50-s period regionalised group velocity map. (**b**) Regionalised group (U) and phase (C) velocities at the 50-s period along the transect from models using basic cells (black), once-partitioned cells (red) and twice-partitioned cells (blue). (**c**) Regionalised group velocity dispersion curves along the transect. (**d**) Regionalised phase velocity dispersion curves along the transect. The grey triangles in (a) denote the cells with adaptive sizes. The black and grey wiggles in (c,d) represent velocities higher and lower than the regional mean at a given period, respectively. The exaggerated topography is provided above the transects in (c,d), with main tectonic blocks labelled. CAOB is the Central Asian Orogenic Belt

thereby implying that fixed-size cells are not adequate for recovering the structures in detail. As expected, the velocities from the once-partitioned cell model (red) reduce this bias. The velocities from our final model (using twice-partitioned cells, blue triangles in Fig. 2b) vary much more smoothly and show greater detail along the transect than the other two models, confirming the advantage of using variable-size cells.

We plotted the regionalised dispersion curves as wiggle traces with the vertical axis corresponding to the period in Fig. 8c and d, to visualise the regionalised dispersion curves at all periods, as Fig. 8b only shows regionalised velocities at one period. The black and grey wiggles indicate positive and negative velocity perturbations relative to the regional mean, respectively, with the magnitude of the wiggle representing the size of the perturbation. Figure 8c gives the regionalised group velocity dispersion curves along transect a–a’. The Sichuan and Tarim basins have negative velocity anomalies at the ~ 10-s period, whereas the Tibetan Plateau has a positive anomaly at this period, which implies that the basins are covered by low-velocity sediments and the plateau is not. In addition, the Tibetan Plateau has a strong low-velocity anomaly at periods of 20–60 s, which is consistent with the very thick crust in the region. Another striking feature of the group velocity transect is that the positive anomalies are consistently observed beneath the old and stable Yangtze and Tarim cratons at periods longer than ~ 50–60 s. The southeastern Tibetan Plateau has a weakly positive to neutral velocity anomaly at periods longer than ~ 90 s, indicating a thicker but weaker lithosphere beneath the plateau relative to the cratonic regions. Figure 8d gives the regionalised phase velocity dispersion curves along transect a–a’. The phase velocity transect captures similar regional features to the group velocity transect, except that the anomalies on the phase velocity transect are located shallower (shorter periods) than those on the group velocity transect. This modelled output is reasonable because the phase waves have longer wavelengths (deeper sensitivities) than the group waves for a given period. The good correlation of our regionalised velocity features with tectonic blocks indicates the reliability of our results.

To demonstrate the feasibility of using adaptive cells in our tomography, we compared our model with Yang et al.'s (2023) regional phase velocity model for SE Tibet. Although our model imaged fewer local-scale features than the model of Yang et al. (2023) as a result of using fewer local measurements, both models imaged consistent regional-scale velocity anomalies. Given that the main objective of our study is to provide updated regionalized dispersion curves for a large region such as East Asia, we did not include as many local measurements as in other regional studies. Additional detail on local structures can be found in regional models (e.g., Zhang et al. 2018; Yang et al. 2023).

We also compared our model with Shen et al.'s (2016) group velocity map of the Chinese mainland at a period of 30 s (Figure S2 in Supplementary Information). An obvious difference between the two studies is that the map of Shen et al. (2016) shows many anomalies of ≤ 100 km in size (1° of great-arc distance), smaller than the average wavelength of 30 s surface waves. The anomaly patches might reflect the node parameterization ($0.5° \times 0.5°$) and smoothing regularization of Shen et al. (2016), which permits velocity varying from node to node at a distance of ~0.5°. In any event, except for the small anomaly patches, our group-velocity model at a period of 30 s compares well with the results of Shen et al. (2016). Furthermore, our model imaged extra features of wide low velocities beneath the Mongolian Plateau and delineated the Qiangtang terrane by a concentrated low-velocity feature.

6 Conclusions

We proposed a new model discretisation approach for surface-wave tomography that divides the study area into triangular cells with variable sizes based on data coverage and that employs a new matched approach for adding regularisation and conducting a resolution evaluation. These approaches were then applied to East Asia and revealed structures with adaptive resolutions. These structures were well delineated, with both the small and large tectonic domains of East Asia being identified, and the quantified resolutions being consistent with the data coverage, thereby implying that tomography using variable-size cells for regions with unevenly distributed observations can better optimise model resolution than tomography using fixed-size cells.

Acknowledgements This study was jointly supported by the Natural Science Foundation of China (42174068, 42430305) and the China Geological Survey (DD20242875). Most of the figures were plotted using Generic Mapping Tools (Wessel et al. 2013).

Author contribution M.F. wrote the main manuscript text. M.A. provided programing support and prepared part of the figures. H.H. got part of the financial support and contributed discussions. R.Z. were involved in method designing and data processing. All authors reviewed the manuscript.

Data availability The seismic data are available from the IRIS Data Management Center (http://ds.iris.edu/ds/nodes/dmc/data/), the National Seismic Network Data Backup Center of the Institute of Geophysics, China Earthquake Administration (https://doi.org/10.11998/SeisDmc/SN), the China Earthquake Science Exploration Array Data Center (https://doi.org/10.12001/ChinArray.Data) and from GEOFON (https://doi.org/https://doi.org/10.14470/7S7567431325). The program used to divide the Earth's surface into equal-sized Delaunay triangulation cells was written by Sahr et al. (2003). The program used to evaluate the resolution was written by An (2012) and can be downloaded from http://seismolab.org/people/meijian/softs/index.html. The regionalised Rayleigh-wave group and phase velocity dispersion curves and their resolution evaluations for East Asia are available in either the Supplementary Information or at http://seismolab.org/model/asia/EA_Rg_UC.dsp.tgz.

Declarations

Competing Interests The authors declare no competing interests.

References

Abers GA, Roecker SW (1991) Deep structure of an arc-continent collision: Earthquake relocation and inversion for upper mantle P and S wave velocities beneath Papua New Guinea. J Geophys Res 96:6379–6401

An M (2012) A simple method for determining the spatial resolution of a general inverse problem. Geophys J Int 191:849–864

An M, Feng M, Zhao Y (2009) Destruction of lithosphere within the north China craton inferred from surface wave tomography. Geochem Geophys Geosyst 10:Q08016

An M, Wiens DA, Zhao Y, Feng M, Nyblade A, Kanao M, Li Y, Maggi A, Lévêque J-J (2015) S-velocity model and inferred Moho topography beneath the Antarctic Plate from Rayleigh waves. J Geophys Res 120:359–383

Backus G, Gilbert F (1968) The resolving power of gross earth data. Geophys J R Astron Soc 16:169–205

Backus G, Gilbert F (1970) Uniqueness in the Inversion of Inaccurate Gross Earth Data. Phil Trans r Soc Lond A 266:123–192

Bird P (2003) An updated digital model of plate boundaries. Geochem Geophys Geosyst 4:1027

Boué P, Roux P, Campillo M, Briand X (2014) Phase velocity tomography of surface waves using ambient noise cross correlation and array processing. J Geophys Res 119:519–529

Carrillo J, Pérez-Flores MA, Calò M (2024) Three-dimensional joint inversion of surface wave dispersion and gravity data using a petrophysical approach: an application to Los Humeros Geothermal Field. Geophys J Int 239:1217–1235

Chang S-J, van der Lee S, Flanagan MP, Bedle H, Marone F, Matzel EM, Pasyanos ME, Rodgers AJ, Romanowicz B, Schmid C (2010) Joint inversion for three-dimensional S velocity mantle structure along the Tethyan margin. J Geophys Res 115:B08309

Chang L, Ding Z, Wang C, Flesch LM (2017) Vertical coherence of deformation in lithosphere in the NE margin of the Tibetan plateau using GPS and shear-wave splitting data. Tectonophysics 699:93–101

Chen L, Jiang M, Yang J, Wei Z, Liu C, Ling Y (2014) Presence of an intralithospheric discontinuity in the central and western North China Craton: Implications for destruction of the craton. Geology 42:223–226

Chevrot S, Villaseñor A, Sylvander M, Benahmed S, Beucler E, Cougoulat G, Delmas P, de Saint Blanquat M, Diaz J, Gallart J, Grimaud F, Lagabrielle Y, Manatschal G, Mocquet A, Pauchet H, Paul A, Péquegnat C, Quillard O, Roussel S, Ruiz M, Wolyniec D (2014) High-resolution imaging of the Pyrenees and Massif Central from the data of the PYROPE and IBERARRAY portable array deployments. J Geophys Res 119:6399–6420

Chiao L-Y, Chen Y-N, Gung Y (2014) Constructing empirical resolution diagnostics for kriging and minimum curvature gridding. J Geophys Res 119:3939–3954

Cho KH, Herrmann RB, Ammon CJ, Lee K (2007) Imaging the Upper Crust of the Korean Peninsula by Surface-Wave Tomography. B Seismol Soc Am 97:198–207

De La Torre TL, Monsalve G, Sheehan AF, Sapkota S, Wu F (2007) Earthquake processes of the Himalayan collision zone in eastern Nepal and the southern Tibetan Plateau. Geophys J Int 171:718–738

Dziewonski AM, Bloch S, Landisman M (1969) A technique for analysis of transient seismic signals. B Seismol Soc Am 59:427–444

Fan J, Bao X, Zhang B (2023) Crustal and upper mantle structure beneath SE China from joint analysis of receiver functions and Rayleigh-wave dispersion. Geophys J Int 235:1798–1809

Feng M, An M (2010) Lithospheric structure of the Chinese mainland determined from joint inversion of regional and teleseismic Rayleigh-wave group velocities. J Geophys Res 115:B06317

Feng M, An M (2013) How to Determine Spatial Resolution for an Inverse Problem (in Chinese with English Abstract). CT Theory and Applications 22:587–604

Feng M, Assumpção MS, van der Lee S (2004) Group-velocity tomography and lithospheric S-velocity structure of the South American continent. Phys Earth Planet in 147:315–331

Feng M, An M, Zhao W, Xue G, Mechie J, Zhao Y (2011) Lithosphere structures of northeast Tibetan Plateau and their geodynamic implications. J Geodynamics 52:432–442

Feng M, An M, Dong S (2017) Tectonic history of the Ordos Block and Qinling Orogen inferred from crustal thickness. Geophys J Int 210:303–320

Feng M, An M, Mechie J, Zhao W, Xue G, Su H (2020) Lithospheric structures of and tectonic implications for the central-east Tibetan plateau inferred from joint tomography of receiver functions and surface waves. Geophys J Int 223:1688–1707

Feng M, Qian H, Mechie J, An M, Li H, Xue G, Su H, Cui X (2021) Crustal seismogenic structures and deformation styles along the Longmen Shan Fault belt in the eastern Tibetan Plateau inferred from ambient noise tomography. Tectonophysics 798:228689

Feng M, An M, Hou H, Fan T, Zang H (2023a) Channelised magma ascent and lithospheric zonation beneath the Songliao Basin, Northeast China, based on surface-wave tomography. Tectonophysics 862:229969

Feng M, An M, Hou H, Fan T, Zang H (2023b) The Lithospheric Structure of the Middle Solonker−Xar Moron Suture by Surface-wave Tomography (in Chinese with English Abstract). CT Theory Appl 32:1–14

Fichtner A, Leeuwen TV (2015) Resolution analysis by random probing. J Geophys Res 120:5549–5573

Fichtner A, Trampert J (2011) Resolution analysis in full waveform inversion. Geophys J Int 187:1604–1624

Fishwick S (2010) Surface wave tomography: Imaging of the lithosphere–asthenosphere boundary beneath central and southern Africa? Lithos 120:63–73

Han S, Zhang H, Gao L, Liu Y, Chai C, Maceira M (2022) Joint Inversion of Body Wave Arrival Times, Surface Wave Dispersion Data and Receiver Functions: Method and Application to South China. J Geophys Res 127:e2022JB024083

Hansen SE, Nyblade AA, Benoit MH (2012) Mantle structure beneath Africa and Arabia from adaptively parameterized P-wave tomography: Implications for the origin of Cenozoic Afro-Arabian tectonism, *Earth Planet*. Sci Lett 319–320:23–34

Hansen SE, Graw JH, Kenyon LM, Nyblade AA, Wiens DA, Aster RC, Huerta AD, Anandakrishnan S, Wilson T (2014) Imaging the Antarctic mantle using adaptively parameterized P-wave tomography: Evidence for heterogeneous structure beneath West Antarctica, *Earth Planet*. Sci Lett 408:66–78

Herrmann RB (2013) Computer Programs in Seismology: An Evolving Tool for Instruction and Research. Seismol Res Lett 84:1081–1088

Isse T, Kawakatsu H, Yoshizawa K, Takeo A, Shiobara H, Sugioka H, Ito A, Suetsugu D, Reymond D (2019) Surface wave tomography for the Pacific Ocean incorporating seafloor seismic observations and plate thermal evolution, *Earth Planet*. Sci Lett 510:116–130

Julià J, Ammon CJ, Herrmann RB, Correig AM (2000) Joint inversion of receiver function and surface wave dispersion observations. Geophys J Int 143:99–112

Kennett BLN, Engdahl ER (1991) Traveltimes for global earthquake location and phase identification. Geophys J Int 105:429–465

Kind R, Yuan X, Saul J, Nelson D, Sobolev SV, Mechie J, Jiang M (2002) Seismic images of crust and upper mantle beneath Tibet: evidence for Eurasian plate subduction. Science 298:1219–1221

Laske G, Masters G, Ma Z, Pasyanos M (2013) Update on CRUST1.0 - A 1-degree Global Model of Earth's Crust. https://igppweb.ucsd.edu/~gabi/crust1.html. Accessed 01 Feb 2025

Lebedev S, Nolet G (2003) Upper mantle beneath Southeast Asia from S velocity tomography. J Geophys Res 108:2048

Lévěque J-J, Rivera L, Wittlinger G (1993) On the use of the checker-board test to assess the resolution of tomographic inversions. Geophys J Int 115:313–318

Li L, Fu YV (2020) Surface-Wave Tomography of Eastern and Central Tibet from Two-Plane-Wave Inversion: Rayleigh-Wave and Love-Wave Phase Velocity Maps. B Seismol Soc Am 110:1359–1371

Li P, Lin G (2014) Adaptive ambient noise tomography and its application to the Garlock Fault, southern California. Geophys J Int 197:1236–1249

Lin F-C, Moschetti MP, Ritzwoller MH (2008) Surface wave tomography of the western United States from ambient seismic noise: Rayleigh and Love wave phase velocity maps. Geophys J Int 173:281–298

Lloyd S, van der Lee S, França GS, Assumpção M, Feng M (2010) Moho map of South America from receiver functions and surface waves. J Geophys Res 115:B11315

Lu Y, Stehly L, Paul A, Group AW (2018) High-resolution surface wave tomography of the European crust and uppermost mantle from ambient seismic noise. Geophys J Int 214:1136−1150

Ma Z, Masters G, Laske G, Pasyanos M (2014) A comprehensive dispersion model of surface wave phase and group velocity for the globe. Geophys J Int 199:113–135

Maceira M, Ammon CJ (2009) Joint inversion of surface wave velocity and gravity observations and its application to central Asian basins shear velocity structure. J Geophys Res 114:B02314

Magrini F, Diaferia G, El-Sharkawy A, Cammarano F, van Der Meijde M, Meier T, Boschi L (2022) Surface-Wave Tomography of the Central-Western Mediterranean: New Insights Into the Liguro-Provençal and Tyrrhenian Basins. J Geophys Res: Solid Earth 127(3):e2021JB023267

Moorkamp M, Jones AG, Fishwick S (2010) Joint inversion of receiver functions, surface wave dispersion, and magnetotelluric data. J Geophys Res 115:B04318

Morozov VA (1984) Methods for solving incorrectly posed problems. Springer-Verlag, New York

Moschetti MP, Ritzwoller MH, Shapiro NM (2007) Surface wave tomography of the western United States from ambient seismic noise: Rayleigh wave group velocity maps. Geochem Geophys Geosyst 8:Q08010

Nishida K, Montagner J-P, Kawakatsu H (2009) Global Surface Wave Tomography Using Seismic Hum. Science 326:112

Nolet G (2008) A breviary of seismic tomography: imaging the interior of the earth and sun. Cambridge University Press, Cambridge, UK

Ojo AO, Ni S, Chen H, Xie J (2018) Crust-mantle coupling mechanism in Cameroon, West Africa, revealed by 3D S-wave velocity and azimuthal anisotropy. Phys Earth Planet in 274:195–213

Paige CC, Saunders MA (1982) Algorithm 583, LSQR: Sparse linear equations and least squares problems, *ACM Trans*. Math Softw 8:195–209

Qian H, Mechie J, Li H, Xue G, Su H, Cui X (2018) Structure of the Crust and Mantle Down to 700 km Depth beneath the Longmenshan From P Receiver Functions. Tectonics 37:1688–1708

Qian H, Yu C, Mechie J, Zeng X (2022) Dense seismological array and profile across the Longmenshan and the deep extension of the Pengguan complex. Tectonophysics 823:229193

Qian H, Mechie J (2012) Temporary seismological network in Longmenshan, China (2012/2013). Deutsches GeoForschungsZentrum GFZ. https://doi.org/10.14470/7S7567431325

Qu P, Chen Y, Yu Y, Gai Z, Li Q, Dong S (2020) 3D velocity structure of upper mantle beneath South China and its tectonic implications: evidence from finite frequency seismic tomography (in Chinese with English abstract), *Chinese*. J Geophys 63:2954–2969

Ramos C, Mechie J, Feng M (2016) Shear wave velocity and Poisson's ratio models across the southern Chile convergent margin at 38°15' S. Geophys J Int 204:1620–1635

Ren J, Niu B, Wang J, Jin X, Zhao L, Liu R (2013) Advances in research of Asian geology—A summary of 1:5M International Geological Map of Asia project. J Asian Earth Sci 72:3–11

Ritzwoller MH, Levshin AL (1998) Eurasian surface wave tomography: Group velocities. J Geophys Res 103:4839–4878

Ritzwoller MH, Shapiro NM, Barmin MP, Levshin AL (2002) Global surface wave diffraction tomography. J Geophys Res 107:2335

Rodríguez Kacevas M, Assumpção M, Sánchez Bettucci L, An M, Feng M (2024) Crustal thicknesses in Uruguay from joint inversion of receiver functions and surface wave dispersion. J S Am Earth Sci 146:105062

Roux E, Moorkamp M, Jones AG, Bischoff M, Endrun B, Lebedev S, Meier T (2011) Joint inversion of long-period magnetotelluric data and surface-wave dispersion curves for anisotropic structure: application to data from Central Germany. Geophys Res Lett 38:L05304

Sahr K, White D, Kimerling AJ (2003) Geodesic Discrete Global Grid Systems. Cartogr Geogr Inf Sc 30:121–134

Sambridge M, Braun J, McQueen H (1995) Geophysical parametrization and interpolation of irregular data using natural neighbours. Geophys J Int 122:837–857

Schaefer JF, Boschi L, Kissling E (2011) Adaptively parametrized surface wave tomography: methodology and a new model of the European upper mantle. Geophys J Int 186:1431–1453

Shen W, Ritzwoller MH, Kang D, Kim Y, Lin F-C, Ning J, Wang W, Zheng Y, Zhou L (2016) A seismic reference model for the crust and uppermost mantle beneath China from surface wave dispersion. Geophys J Int 206:954–979

Sieminski A, Lévêque J-J, Debayle E (2004) Can finite-frequency effects be accounted for in ray theory surface wave tomography? Geophys Res Lett 31:L24614

Sun X, Bao X, Xu M, Eaton DW, Song X, Wang L, Ding Z, Mi N, Yu D, Li H (2014) Crustal structure beneath SE Tibet from joint analysis of receiver functions and Rayleigh wave dispersion. Geophys Res Lett 41:1479–1484

Syracuse EM, Zhang H, Maceiraac M (2017) Joint inversion of seismic and gravity data for imaging seismic velocity structure of the crust and upper mantle beneath Utah United States. Tectonophys 718:105–117

Tao K, Niu F, Ning J, Chen YJ, Grand S, Kawakatsu H, Tanaka S, Obayashi M, Ni J (2014) Crustal structure beneath NE China imaged by NECESSArray receiver function data, *Earth Planet*. Sci Lett 398:48–57

Thurber C, Eberhart-Phillips D (1999) Local earthquake tomography with flexible gridding. Comput Geosci 25:809–818

Tilmann F, Ni J, INDEPTH III Seismic Team (2003) Seismic imaging of the downwelling indian lithosphere beneath central Tibet. Science 300:1424−1427

Trampert J, Woodhouse JH (1995) Global phase velocity maps of Love and Rayleigh waves between 40 and 150 seconds. Geophys J Int 122:675–690

Trampert J, Woodhouse JH (2001) Assessment of global phase velocity models. Geophys J Int 144:165–174

Vdovin O, Rial JA, Levshin AL, Ritzwoller MH (1999) Group-velocity tomography of South America and the surrounding oceans. Geophys J Int 136:324–340

Wang Z, Dahlen FA (1995) Spherical-spline parameterization of three-dimensional earth models. Geophys Res Lett 22:3099–3102

Wang Z, Tromp J, Ekström G (1998) Global and regional surface-wave inversions: A spherical-spline parameterization. Geophys Res Lett 25:207–210

Wang X, Chen QF, Li J, Wei S (2016) Seismic Sensor Misorientation Measurement Using P-Wave Particle Motion: An Application to the NECsaids Array. Seismol Res Lett 87:901–911

Wei Z, Chen L, Xu W (2011) Crustal thickness and Vp/Vs ratio of the central and western North China Craton and its tectonic implications. Geophys J Int 186:385–389

Wessel P, Smith WHF, Scharroo R, Luis J, Wobbe F (2013) Generic Mapping Tools: Improved version released. EOS Trans Am Geophys Union 94:409–410

Wittlinger G, Farra V, Hetenyi G, Vergne J, Nabelek J (2009) Seismic velocities in Southern Tibet lower crust: a receiver function approach for eclogite detection. Geophys J Int 177:1037–1049

Wu P, Tan H, Lin C, Peng M, Ma H, Yan Z (2020) Joint inversion of two-dimensional magnetotelluric and surface wave dispersion data with cross-gradient constraints. Geophys J Int 221:938–950

Yang X, Luo Y, Jiang C, Yang Y, Niu F, Li G (2023) Crustal and Upper Mantle Velocity Structure of SE Tibet From Joint Inversion of Rayleigh Wave Phase Velocity and Teleseismic Body Wave Data. J Geophys Res 128**:**e2022JB026162.

Yin A (2010) Cenozoic tectonic evolution of Asia: A preliminary synthesis. Tectonophysics 488:293–325

Yue H, Chen YJ, Sandvol E, Ni J, Hearn T, Zhou S, Feng Y, Ge Z, Trujillo A, Wang Y, Jin G, Jiang M, Tang Y, Liang X, Wei S, Wang H, Fan W, Liu Z (2012) Lithospheric and upper mantle structure of the northeastern Tibetan Plateau. J Geophys Res 117:B05307

Zhang F, Wu Q, Li Y, Zhang R, Sun L, Pan J, Ding Z (2018) Seismic Tomography of Eastern Tibet: Implications for the Tibetan Plateau Growth. Tectonics 37:2833–2847

Zhang K, Chen Q, Chen Y (2020) Crustal structure beneath the southwestern Xing'an-Mongolia Orogenic Belt revealed by receiver function analysis (in Chinese with English Abstract), *Chinese*. J Geophys 63:1–21

Zhao W, Kumar P, Mechie J, Kind R, Meissner R, Wu Z, Shi D, Su H, Xue G, Karplus M, Tilmann F (2011) Tibetan plate overriding the Asian plate in central and northern Tibet. Nat Geosci 4:870–873

Zheng XF, Yao ZX, Liang JH, Zheng J (2010) The role played and opportunities provided by IGP DMC of China National Seismic Network in Wenchuan earthquake disaster relief and researches. B Seismol Soc Am 100:2866–2872

Zhou Z, Wiens DA, Shen W, Aster RC, Nyblade A, Wilson TJ (2022) Radial Anisotropy and Sediment Thickness of West and Central Antarctica Estimated From Rayleigh and Love Wave Velocities. J Geophys Res 127:e2021JB022857